





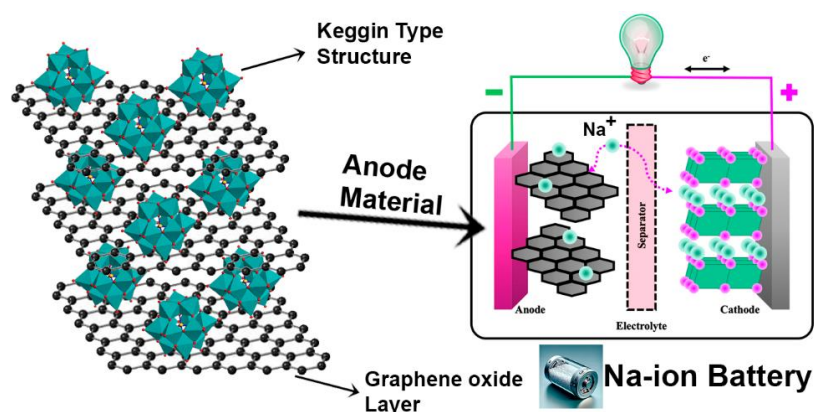
Full Paper | <http://dx.doi.org/10.17807/orbital.v17i2.21046>

Synthesis and Characterization of a New Keggin-Type Polyoxoniobate for Application as Anodes in Sodium-ion Batteries (SIBs)

Alan Fernando Yoshiaki Matsushita* ^a, Josias do Rocio Vitor do Nascimento ^a, João Manoel de Aguiar Leite ^a, and Jarem Raul Garcia ^a

In the pursuit of sustainable energy solutions and advancements in energy storage technology, this research focuses on the synthesis, characterization, and electrochemical evaluation of a Keggin-Type polyoxoniobate compound for potential application in sodium-ion batteries (SIBs). While lithium-ion batteries have been the standard, concerns about lithium availability and environmental issues have prompted the exploration of alternative materials for SIBs. Polyoxoniobates, a subclass of polyoxometalates, have unique properties that make them promising candidates for the development of high-performance SIBs. This study delves into the relatively uncharted territory of polyoxoniobates in SIBs. The research investigates the adaptation of polyoxoniobate structures to enhance their electrochemical properties, the understanding of sodium ion storage mechanisms, and comprehensive characterization. A specific Keggin-Type polyoxoniobate compound is synthesized and examined for its potential as an electrode material for SIBs. The structural analysis confirms the successful synthesis of the compound, with X-ray diffraction patterns, Raman spectroscopy, and FTIR spectra demonstrating its purity and integrity. Scanning electron microscopy reveals the unique morphology of the composite material, indicating interactions between graphene oxide (GO) and polyoxoniobates. Elemental analysis further confirms the composition of the composite material, aligning with the expected stoichiometry. Electrochemical characterization using various techniques, including cyclic voltammetry, chronopotentiometry charge/discharge, and electrochemical impedance spectroscopy, provides insights into the electrochemical behavior of the synthesized material. These findings contribute to the understanding of structure-activity relationships in polyoxoniobates and their potential as crucial components in future SIBs.

Graphical abstract



Keywords

Energy storage
Niobium
Polyoxometalates
Sodium ion batteries

Article history

Received 01 May 2024
Revised 08 Aug 2024
Accepted 04 Sep 2024
Available online 18 May 2025

Handling Editor: Sergio L. Lazaro

^a Departament of Chemistry, State University of Ponta Grossa (UEPG). Av. Gal. Carlos Cavalcanti, 4748 – Uvaranas, Ponta Grossa, PR, Brazil, 84030-900. *Corresponding author. E-mail: alanmatsushita@hotmail.com

1. Introduction

The increasing demand for sustainable energy solutions and the continuous pursuit of advancements in energy storage technology have stimulated the exploration of novel materials for sodium-ion battery applications. While lithium-ion batteries dominate the energy storage industry, concerns about limited lithium availability, alongside the environmental and economic implications of its extraction have prompted research into more accessible and eco-friendly alternatives [1–4]. In this context, polyoxometalates (POMs) are recognized as promising candidates due to their unique properties that contribute to the development of next-generation high-performance sodium-ion batteries (SIBs) [5].

Recently, interest in polyoxometalates as electrode materials in sodium-ion batteries has grown substantially due to their flexible redox properties and ability to form diverse structures. Priyadarshini et al. (2021) showed that Keggin-type polyoxometalates, specifically $\text{Na}_5\text{PMo}_{10}\text{V}_2\text{O}_{40}$, exhibit remarkable multi-electron redox properties and have been employed as cathode materials in SIBs. In this study, it was observed that the redox potential of POM can be tuned by varying the counterion, heteroatoms and transition metals in the cluster. Furthermore, the material demonstrated promising results in terms of specific capacity and stability, associated with the multi-electron redox reaction of $\text{Mo}^{6+}/\text{Mo}^{4+}$ and $\text{V}^{5+}/\text{V}^{4+}$. DFT studies indicated that the less-bound sodium ions, upon intercalation into the intercluster cavities, improve the electrochemical behavior of the material [6].

Hartung et al. (2015) explored vanadium-based polyoxometalates, specifically $\text{Na}_6[\text{V}_{10}\text{O}_{28}] \cdot 16\text{H}_2\text{O}$, as potential anode materials in sodium-ion batteries. This compound was synthesized and characterized, demonstrating high capacity and cyclic stability when used as an anode material. The research suggests that this high stability is attributed to the insertion of sodium ions between the $[\text{V}_{10}\text{O}_{28}]^{6-}$ anions, rather than an intercalation in a continuous crystal structure. This mechanism reduces the strain in the crystal structures, providing a promising avenue for improving battery durability and performance [7].

Despite significant advances in the use of polyoxometalates in sodium-ion batteries, research continues to expand into specific subclasses that may offer even more advantageous properties. Polyoxoniobates, a subclass of polyoxometalates, have attracted significant attention within the scientific community for their complex polyhedral structures and versatile electrochemical characteristics. Although these compounds have primarily been studied within the context of catalysis and photocatalysis [8, 9], their potential in energy storage, especially in sodium-ion batteries is not yet fully explored. The integration of their inherent structural and electrochemical properties suggests that polyoxoniobates could serve as the basis for developing innovative electrode materials.

Although there is increasing interest, the application of polyoxoniobates in sodium-ion batteries is still emerging. Adapting polyoxoniobate structures to enhance their electrochemical properties, understanding the mechanisms of sodium ion storage and release, and thoroughly characterizing their physical and electrochemical attributes present significant scientific challenges [10, 11]. Addressing

these knowledge gaps is crucial for advancing polyoxoniobates as electrodes in sodium-ion batteries.

This research focuses on the synthesis, structural characterization, and electrochemical evaluation of a specific Keggin-Type polyoxoniobate compound, aiming to elucidate its performance as an electrode material for sodium-ion batteries. The Keggin-type structure, a prominent class of polyoxometalates (POMs) features a unique molecular architecture with a central tetrahedral core, typically composed of phosphorus or silicon, surrounded by oxygen groups that create a 'window' encapsulating metal atoms. This anionic cluster, capable of exchanging cations, is used in various commercial applications due to its compelling chemical properties and exceptional stability. Its ability to transition to higher oxidation states makes it suitable for use as both an electrolyte and electrodes in energy storage systems [12–15]. Moreover, this structure provides an accessible surface for charge transfer, highlighting its potential in the development of new materials for sodium-ion batteries. Thus, Keggin-type structures of polyoxometalates play a vital role in advancing energy storage technology.

This study aims to offer significant insights into the structure-activity relationships of polyoxoniobates and their potential as crucial components in the sodium-ion batteries SIBs.

2. Material and Methods

2.1 Chemical Materials

All chemicals were commercially available and used without further purification. Amorphous niobium pentoxide (Nb_2O_5 99.8% purity) was received via Brazilian Metallurgy and Mining Company (CBMM) donation.

Carbon Black was purchased from Cabotcorp and Sodium Sulfate (Na_2SO_4), polyvinylidene (PVDF), n-methyl pyrrolidone (NMP), Potassium Hydroxide (KOH) and Tetraethyl orthosilicate (TEOS) were purchased from Sigma-Aldrich (Germany). Milli-Q water was used in all experiments.

2.2 Synthesis of $[\text{H}_2\text{Si}_4\text{Nb}_{16}\text{O}_{56}]$ and $[\text{H}_2\text{Si}_4\text{Nb}_{16}\text{O}_{56}]\text{-GO}$

$\text{H}_2\text{Si}_4\text{Nb}_{16}\text{O}_{56}$ was prepared according to the method reported in the literature [16]. Graphene oxide (GO) was synthesized through an electrochemical exfoliation process within an electrochemical cell comprising a two-electrode system. Na_2SO_4 was employed as the supporting electrolyte, while exposed graphite derived from depleted dry cells was utilized as both the working and counter electrodes. The comprehensive procedural details are safeguarded under patent (BR 10 2013 019478 6). For the $\text{H}_2\text{Si}_4\text{Nb}_{16}\text{O}_{56}\text{-GO}$ composite synthesis, the same procedure employed for $\text{H}_2\text{Si}_4\text{Nb}_{16}\text{O}_{56}$ was utilized, with the addition of graphene oxide in a proportion of 1% to the reaction medium. This led to the formation of the desired composite, as schematically illustrated in Figure 1. The incorporation of graphene oxide imparts specific properties to the composite, contributing to its distinct characteristics and unique performance.

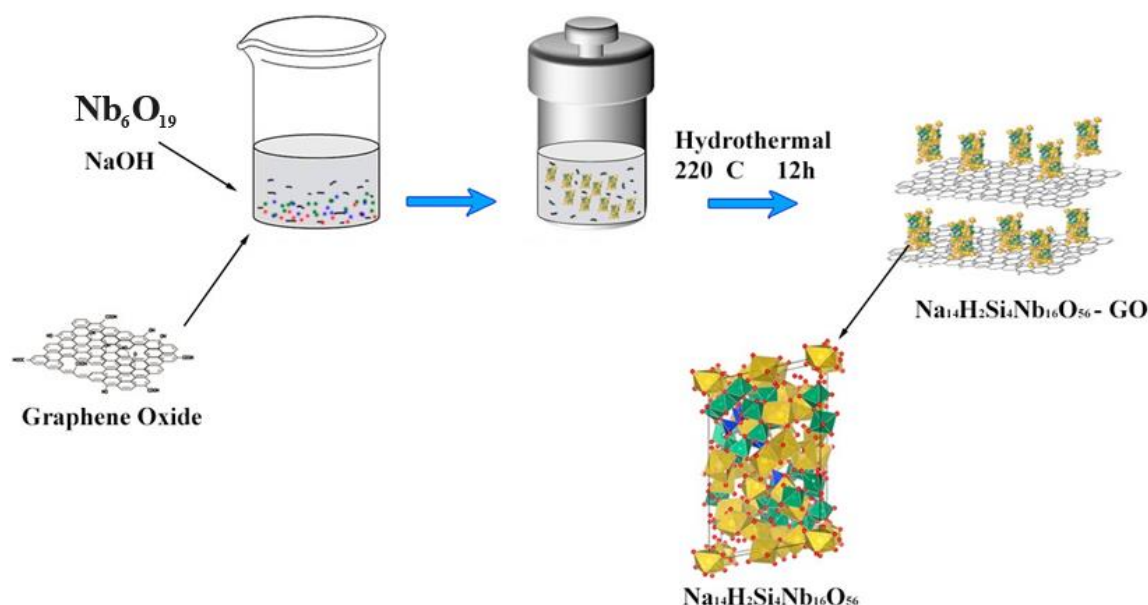


Fig. 1. The schematic illustration of $\text{H}_2\text{Si}_4\text{Nb}_{16}\text{O}_{56}$ and $\text{H}_2\text{Si}_4\text{Nb}_{16}\text{O}_{56}$ -GO composites.

2.3 Characterization

The X-ray diffraction patterns of the synthesized materials were determined by a Rigaku Ultima IV diffractometer using CuK α radiation ($\lambda = 1.5406 \text{ \AA}$) operated at 40 kV/30 mA. The diffraction patterns were recorded using 0.02° per step and 1° min^{-1} in the range $5^\circ < 2\theta < 75^\circ$.

Raman shift spectroscopy of the samples was recorded by BRUKER Senterra using a 532 nm laser source and an excitation power of 20 mW.

Attenuated reflection infrared spectroscopy (ATR-FTIR) was performed in a Shimadzu / IRPrestige-21Spectrometer, with wavenumber ranging from 400 to 4000 cm^{-1} . High Resolution Scanning Electronic Microscopy (HR-SEM) micrographs were obtained using a Tescan Mira 3 scanning electron microscope, operating under low vacuum at 2kV. Elemental analysis on microscopic sections of composites was performed by Energy Dispersive Spectroscopy – Tescan.

The electrochemical characterization was performed in a three-electrode cell connected to a Potentiostat/Galvanostat Methrom Autolab model M204, equipped with electrochemical impedance module FRA32, using an Ag/AgCl (3 M) reference electrode and A platinum (Pt) foil with an area of 1 cm^2 was used as auxiliary electrode. The electrochemical behavior of the obtained materials was characterized through a series of electrochemical techniques, including cyclic voltammetry (CV), chronopotentiometry charge/discharge (CD), and electrochemical impedance spectroscopy (EIS) measurements.

In the context of cyclic voltammetry (CV) experiments, the measurements involved the dynamic polarization of the working electrode within the voltage range of -0.5 to 0.5 V (vs. Ag/AgCl) at a scanning rate of 5 mV s^{-1} . The chronopotentiometry charge/discharge (CD) tests were carried out by applying various current densities (30, 50 and 200 mAh g^{-1}) to the working electrode for both charging and discharging cycles. The cutoff potential was set at the threshold values of -0.8 V and 1 V (vs. Ag/AgCl). The electrochemical impedance spectroscopy (EIS) investigations were conducted with the open circuit potential (OCP) applied after 600 seconds of stabilization. An alternating current (AC) perturbation was introduced within a frequency spectrum

spanning from 105 to 0.1 Hz, encompassing 27 frequencies per decade, and utilizing a potential amplitude of 0.01 mV.

For all electrochemical measurements, the support electrolyte used was a 0.5 mol L^{-1} Na_2SO_4 solution at pH 4. The working electrode (WE) fabrication involved mixing 80 wt.% of the active material, 10 wt.% of polyvinylidene fluoride and 10 wt.% of carbon black in 1.0 mL of N-methyl pyrrolidinone. This mixture underwent 30 minutes of ultrasonic irradiation. Subsequently, the resulting slurry was dripped onto the surface of a glassy carbon electrode and dried in an oven at 60 $^\circ\text{C}$.

3. Results and Discussion

The X-ray diffraction patterns of the GO, $\text{H}_2\text{Si}_4\text{Nb}_{16}\text{O}_{56}$, and $\text{H}_2\text{Si}_4\text{Nb}_{16}\text{O}_{56}$ -GO samples are depicted in Figure 2. In the case of GO, a distinct diffraction peak is observed at 26.27 degrees with an interlayer d-spacing of 3.48 \AA . When comparing these values to those reported for pure graphite in the literature, the slightly lower 2θ angle observed in the GO sample, along with the larger d-spacing, suggests a degree of functionalization and disorder in the graphene layers [17,18]. In GO diffractogram (Fig. 2), a broad diffraction peak is observed at $2\theta = 8.7^\circ$, indicating a significant increase in d-spacing. This new peak is consistent with the introduction of oxygen-containing functional groups, such as hydroxyl, carboxyl, carbonyl groups and epoxy into the interlayer space of graphite, which aligns with previously reported values for similar materials [19,20]. The compound $\text{H}_2\text{Si}_4\text{Nb}_{16}\text{O}_{56}$ exhibits sharp diffraction peaks, in accordance with the X-ray diffraction (XRD) patterns previously simulated (Fig. S1) and documented in the literature, confirming the phase purity and good crystallinity [16]. In the case of the $\text{H}_2\text{Si}_4\text{Nb}_{16}\text{O}_{56}$ -GO composite, it is observed that the X-ray diffraction peaks show remarkable similarity to those observed for pure $\text{H}_2\text{Si}_4\text{Nb}_{16}\text{O}_{56}$. It is worth noting that, in the presence of GO in $\text{H}_2\text{Si}_4\text{Nb}_{16}\text{O}_{56}$, a slight reduction in the intensity of the diffraction peaks is noticeable, which corroborates the formation of the $\text{H}_2\text{Si}_4\text{Nb}_{16}\text{O}_{56}$ -GO composite material.

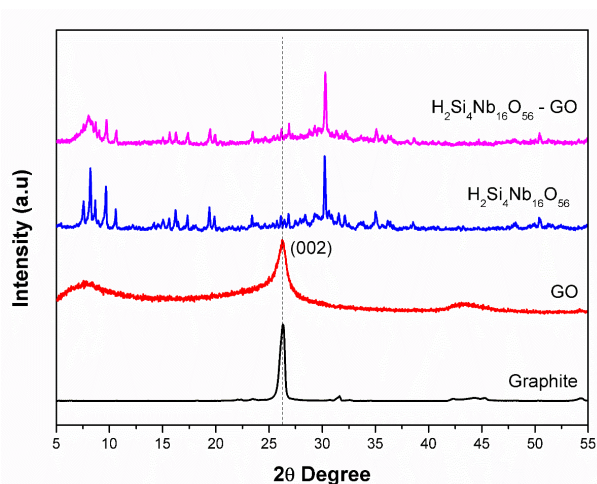


Fig. 2. XRD powder patterns of Graphite, GO, $\text{H}_2\text{Si}_4\text{Nb}_{16}\text{O}_{56}$ and $\text{H}_2\text{Si}_4\text{Nb}_{16}\text{O}_{56}\text{-GO}$.

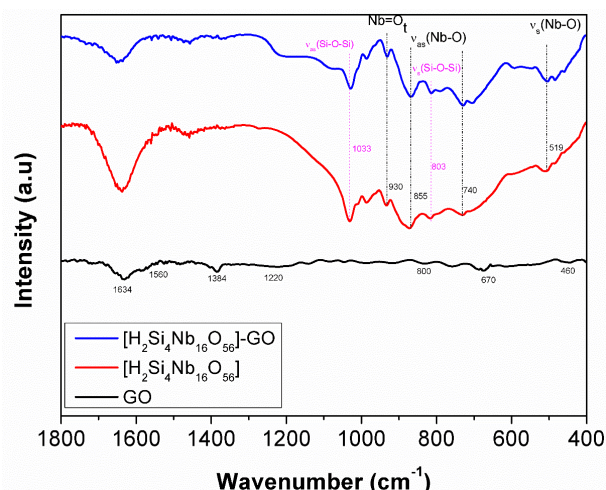


Fig. 3. FTIR spectra of GO, $\text{H}_2\text{Si}_4\text{Nb}_{16}\text{O}_{56}$ and $\text{H}_2\text{Si}_4\text{Nb}_{16}\text{O}_{56}\text{-GO}$.

To further confirm the compositions of the composites, we determined the FT-IR spectra of GO, $\text{H}_2\text{Si}_4\text{Nb}_{16}\text{O}_{56}$, and $\text{H}_2\text{Si}_4\text{Nb}_{16}\text{O}_{56}\text{-GO}$ (Fig. 3). For GO, the spectrum displayed vibrational groups of the GO layer, including peaks at 1634 cm^{-1} corresponding to C=O bonds, 1560 cm^{-1} indicative of C=C sp^2 hybridization, 1384 cm^{-1} arising from C-O and C-OH groups, 1220 cm^{-1} associated with C-O-C bonds, and several peaks at 800, 670, and 460 cm^{-1} corresponding to C-H bending vibrations [21–23]. The FT-IR spectrum of $\text{H}_2\text{Si}_4\text{Nb}_{16}\text{O}_{56}$ revealed distinctive bands, the characteristic Nb=O bond bands appearing near 930 cm^{-1} , as well as peaks at 855 cm^{-1} and 740 cm^{-1} corresponding to asymmetric stretching of the Nb-O bond, and a notable band at 519 cm^{-1} , signifying symmetric stretching of the Nb-O bond. Additionally, it displayed bands at 803 and 1033 cm^{-1} are respectively attributed to the symmetric and asymmetric stretching vibrations of Si-O-Si [24–26]. All characteristic peaks of $\text{H}_2\text{Si}_4\text{Nb}_{16}\text{O}_{56}$ and GO were observed in the $\text{H}_2\text{Si}_4\text{Nb}_{16}\text{O}_{56}\text{-GO}$ composite sample, confirming the structural integrity and purity of both materials.

The Raman spectra of GO, $\text{H}_2\text{Si}_4\text{Nb}_{16}\text{O}_{56}$, and $\text{H}_2\text{Si}_4\text{Nb}_{16}\text{O}_{56}\text{-GO}$ are presented in Figure 4. The GO spectrum exhibited prominent G band (1344 cm^{-1}), indicative of the ordered and pure graphite sheet structure, D band (1597 cm^{-1}), signifying typical defects and impurities in nanostructures and carbon, as well as the 2D band (2670 cm^{-1}), characteristic of graphene structures. To assess the graphene quality, we calculated the ID/IG and I2D/IG ratios for the D, 2D, and G bands, as they directly depend on graphene's layer organization. The GO sample showed ID/IG and I2D/IG ratios of 1.174 and 0.432, respectively. These values, therefore, suggest the formation of multilayer graphene (more than 5 layers) [27–29].

The composite $\text{H}_2\text{Si}_4\text{Nb}_{16}\text{O}_{56}$ exhibited peaks at 776 cm^{-1} and 900 cm^{-1} , which were assigned to the edge-shared octahedral NbO_6 stretching mode and Nb=O terminal stretching mode (terminal bonds possessing double bond character), while the modes at 337 cm^{-1} and 243 cm^{-1} were attributed to the Nb-O stretching mode and Nb-O-Nb bending mode, respectively [30]. Upon comparing the Raman spectra of $\text{H}_2\text{Si}_4\text{Nb}_{16}\text{O}_{56}$ and $\text{H}_2\text{Si}_4\text{Nb}_{16}\text{O}_{56}\text{-GO}$, it is evident that the same bands are identifiable. However, the $\text{H}_2\text{Si}_4\text{Nb}_{16}\text{O}_{56}\text{-GO}$ composite also exhibits the D and G bands characteristic of graphene, which corroborate the material formation in the presence of graphene oxide layers.

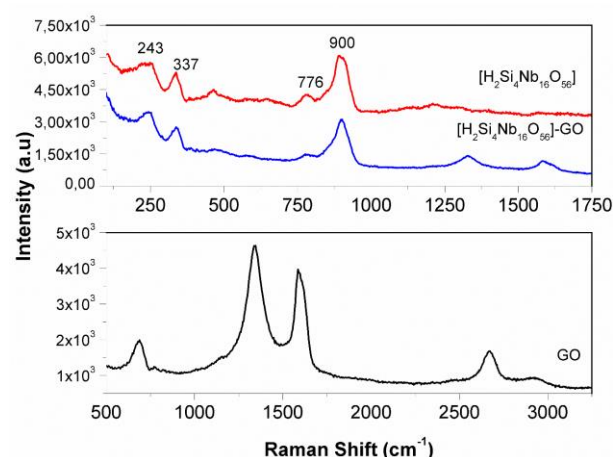


Fig. 4. Raman spectra of GO, $\text{H}_2\text{Si}_4\text{Nb}_{16}\text{O}_{56}$ and $\text{H}_2\text{Si}_4\text{Nb}_{16}\text{O}_{56}\text{-GO}$.

The morphology of the GO (graphene oxide), $\text{H}_2\text{Si}_4\text{Nb}_{16}\text{O}_{56}$, and $\text{H}_2\text{Si}_4\text{Nb}_{16}\text{O}_{56}\text{-GO}$ composites was comprehensively analyzed by scanning electron microscopy (SEM), and elemental mapping. The structure of $\text{H}_2\text{Si}_4\text{Nb}_{16}\text{O}_{56}$ was found to be composed of large irregular pieces, consisting of numerous small interconnected particles. In contrast, GO exhibited a distinctive layered morphology, characterized by a layered arrangement. This layered arrangement of GO is a direct outcome of the exfoliation process, in which graphene sheets are effectively separated and dispersed. The $\text{H}_2\text{Si}_4\text{Nb}_{16}\text{O}_{56}\text{-GO}$ composite, on the other hand, exhibits an agglomerated particle structure with some fine strands formed, which can be attributed to the interaction between GO and $\text{H}_2\text{Si}_4\text{Nb}_{16}\text{O}_{56}$. This unique structure arises from the intrinsic properties of graphene oxide (GO) and the specific nature of the host matrix, $\text{H}_2\text{Si}_4\text{Nb}_{16}\text{O}_{56}$. GO sheets have a high surface area and exhibit a strong tendency to form hydrogen bonds and Van der Waals interactions with neighboring particles [31–33]. When incorporated into the $\text{H}_2\text{Si}_4\text{Nb}_{16}\text{O}_{56}$ matrix, these interactions can lead to the agglomeration of GO sheets and the formation of thin wires due to these interactions. Furthermore, functional groups on the surface of GO can promote the adhesion and aggregation of GO sheets onto particles.

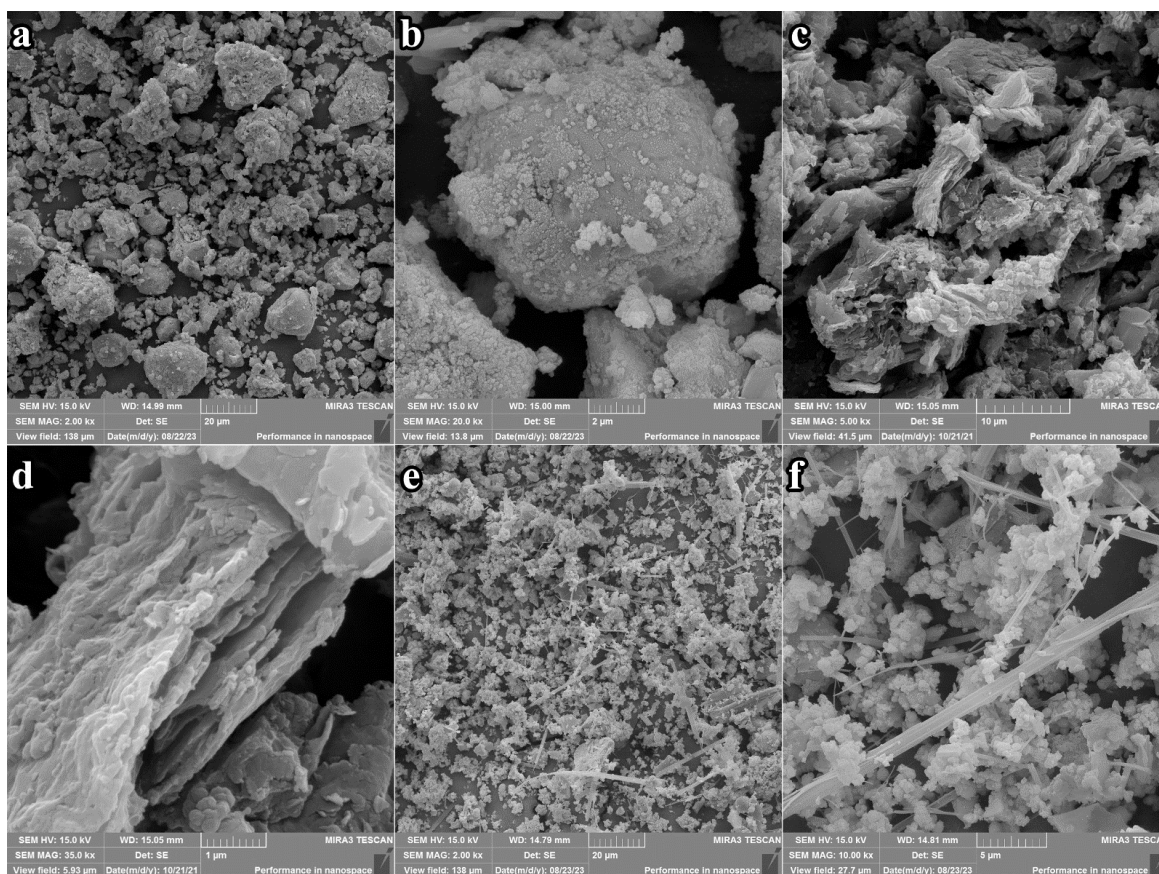


Fig. 5. SEM images of a,b) $\text{H}_2\text{Si}_4\text{Nb}_{16}\text{O}_{56}$, c,d) GO and e,f) $\text{H}_2\text{Si}_4\text{Nb}_{16}\text{O}_{56}$ -GO.

The EDS analysis of the composite revealed the presence of several elements, with weight percentages as follows: oxygen (O) at 34.52%, sodium (Na) at 10.17%, silicon (Si) at 3.56%, and niobium (Nb) at 51.74%. These results are noteworthy as they align well with the expected composition of $\text{Na}_{14}[\text{H}_2\text{Si}_4\text{Nb}_{16}\text{O}_{56}]$, reinforcing the structural integrity and composition of the composite material. $\text{Na}_{14}[\text{H}_2\text{Si}_4\text{Nb}_{16}\text{O}_{56}]$ is a complex inorganic compound consisting of silicon (Si), niobium (Nb), and oxygen (O) atoms in a specific stoichiometry. This underscores the importance of precise compositional analysis in understanding the structure and properties of such complex inorganic compounds.

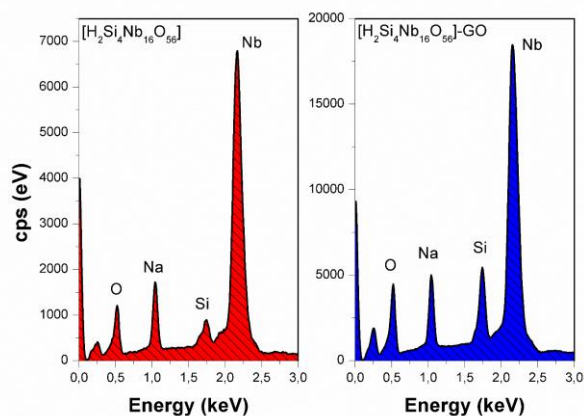


Fig. 6. EDS spectra of $\text{H}_2\text{Si}_4\text{Nb}_{16}\text{O}_{56}$ and $\text{H}_2\text{Si}_4\text{Nb}_{16}\text{O}_{56}$ -GO.

The analysis of elemental maps has enriched our understanding of the samples characteristics. The results of these elemental maps align consistently with observations

obtained through scanning electron microscopy (SEM). The homogeneous distribution of the identified elements, as evidenced by the elemental maps, underscores the uniformity and quality of the sample. This uniformity is of particular significance as it suggests that the elements in question are evenly distributed throughout the sample matrix, including in the $\text{H}_2\text{Si}_4\text{Nb}_{16}\text{O}_{56}$ -GO sample, which exhibited a distinct morphology.

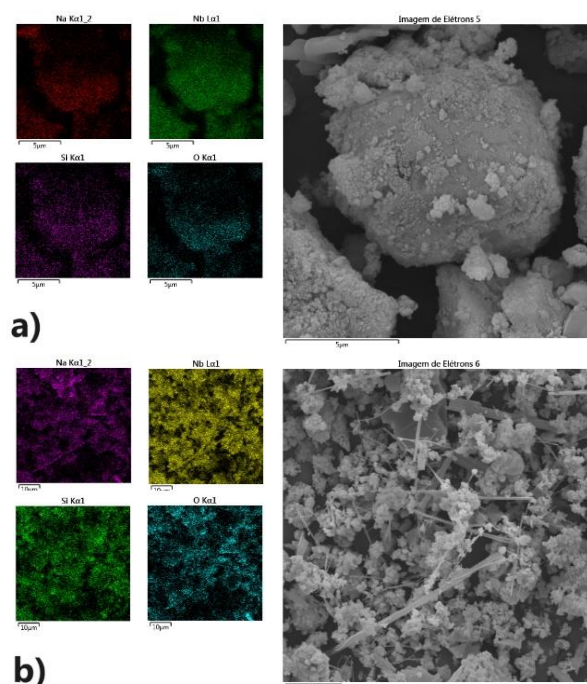


Fig. 7. Elemental maps of $\text{H}_2\text{Si}_4\text{Nb}_{16}\text{O}_{56}$ and $\text{H}_2\text{Si}_4\text{Nb}_{16}\text{O}_{56}$ -GO.

The electrochemical behaviour of the $\text{H}_2\text{Si}_4\text{Nb}_{16}\text{O}_{56}$ and the $\text{H}_2\text{Si}_4\text{Nb}_{16}\text{O}_{56}\text{-GO}$ were evaluated by cyclic voltammetry (CV) measurements were performed with scan rate of 5 and 25 $\text{mV}\cdot\text{s}^{-1}$ over a voltage range of -0.5 and 0.5 V versus $\text{Ag}/\text{AgCl}_{(\text{sat})}$ (showed in Figure 8-a) and 8-c)) and with a scan rate of 25 $\text{mV}\cdot\text{s}^{-1}$ over a voltage range of -1.5 and 0.5 V versus $\text{Ag}/\text{AgCl}_{(\text{sat})}$ (showed in Figure 8-b) and 8-d)).

Figure 8-a), shows the second cycle of the CV measurement for the $\text{H}_2\text{Si}_4\text{Nb}_{16}\text{O}_{56}$ with two different scan rates. At the CV recorded at 5 $\text{mV}\cdot\text{s}^{-1}$ it can be seen an anodic current peak at 0.09 V, which presents a cathodic counterpart at -0.44 V (a broad reduction peak). This redox process could be assigned to the desodiation/sodiation process of the $\text{H}_2\text{Si}_4\text{Nb}_{16}\text{O}_{56}$ probably due to the redox process of the Nb metallic centres [34]. However, when the scan rate is increased to 25 $\text{mV}\cdot\text{s}^{-1}$, this peak current vanishes, indicating a poor kinetic to the electron transfer process. However, from the CV obtained for the $\text{H}_2\text{Si}_4\text{Nb}_{16}\text{O}_{56}\text{-GO}$ (Figure 8-c)) the redox process associated to the desodiation/sodiation process can be observed either in the voltammograms obtained at 5 $\text{mV}\cdot\text{s}^{-1}$ and at 25 $\text{mV}\cdot\text{s}^{-1}$, with the cathodic peak current at -0.32 V and the anodic peak at 0.14 V (versus $\text{Ag}/\text{AgCl}_{(\text{sat})}$). This behaviour indicated that the production of the $\text{H}_2\text{Si}_4\text{Nb}_{16}\text{O}_{56}\text{-GO}$ enhances the kinetic of the redox reaction occurred with the Nb centres. Figures 8-b) and 8-d) show the voltammogram for $\text{H}_2\text{Si}_4\text{Nb}_{16}\text{O}_{56}$ and the $\text{H}_2\text{Si}_4\text{Nb}_{16}\text{O}_{56}\text{-GO}$, respectively, obtained with scan rate of 25 $\text{mV}\cdot\text{s}^{-1}$ over a voltage range of -1.5 and 0.5 V versus $\text{Ag}/\text{AgCl}_{(\text{sat})}$. It is possible to verify that the composite material with GO decrease the current assigned to the hydrogen evolution when compared to the pristine. Also, it was observed, for both material the first cycle is different from the others (not shown). We have performed 5 cycles and from the second to the fifth there is no great difference between them, however the first cycle presents an intense cathodic process at -0.38 V that disappears in the others cycles. This fact can be related to the irreversible electrolyte decomposition, and the irreversible Na-ion insertion in the defects of crystal lattice electrolyte penetration and formation of a solid electrolyte interphase layer (SEI) [35]. The repeatable CV curves confirm the stability and reversibility of the produced electrode.

Figure 9 shows the Nyquist plots for the prepared materials compare to the diagram obtained for an electrode prepared with only CB, which is the material used to insert electronic conductive to the electrode. The measurements were obtained before and after the performing of the Charge-Discharge measurements (C-D). For the CB, the Nyquist diagram shows a vertical strait line, that is a typical profile for a Double Layer Supercapacitor. For the both prepared materials there is observed a depressed semicircle at low frequencies, and a straight line in the high frequency regime. These plots can be qualitatively analysed. The pristine $\text{H}_2\text{Si}_4\text{Nb}_{16}\text{O}_{56}$ material presents a highest resistance for charge transfer (R_{ct}) when compared to the $\text{H}_2\text{Si}_4\text{Nb}_{16}\text{O}_{56}\text{-GO}$ composites, either before and after Charge-Discharge measurements. The straight line in the high frequency region represents the diffusion of Na^+ ions into the bulk electrode. After C-D measurement, this straight line displays a most vertical form, for both materials. These results highlight the enhanced charge transfer process after the formation of the SEI.

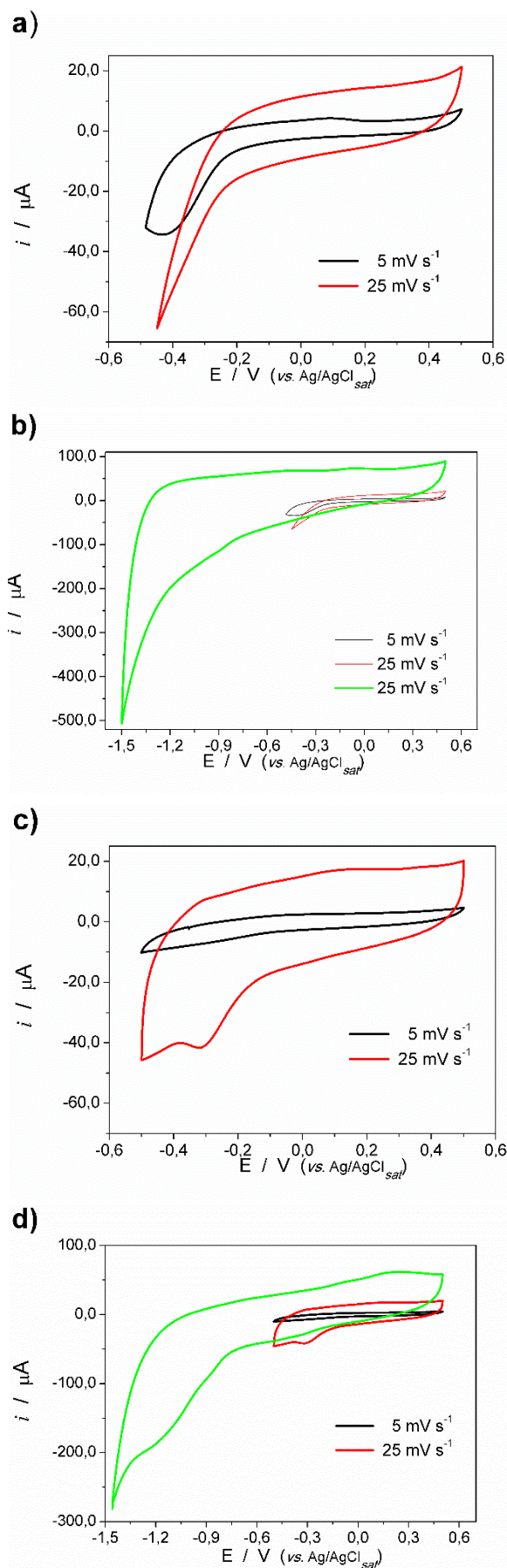


Fig. 8. Cyclic Voltammetry results for the a), b) $\text{H}_2\text{Si}_4\text{Nb}_{16}\text{O}_{56}$ and c), d) $\text{H}_2\text{Si}_4\text{Nb}_{16}\text{O}_{56}\text{-GO}$ over different ranges.

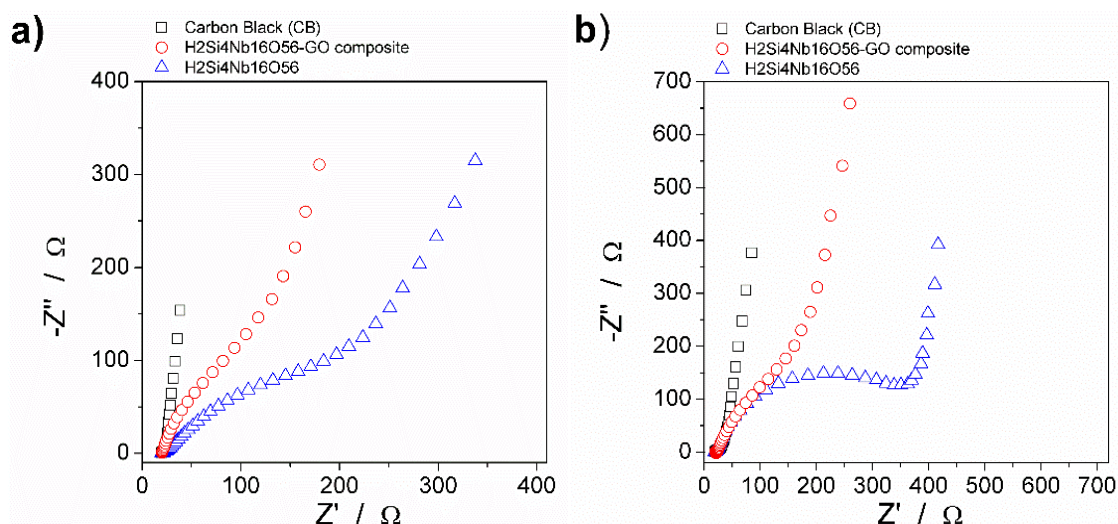
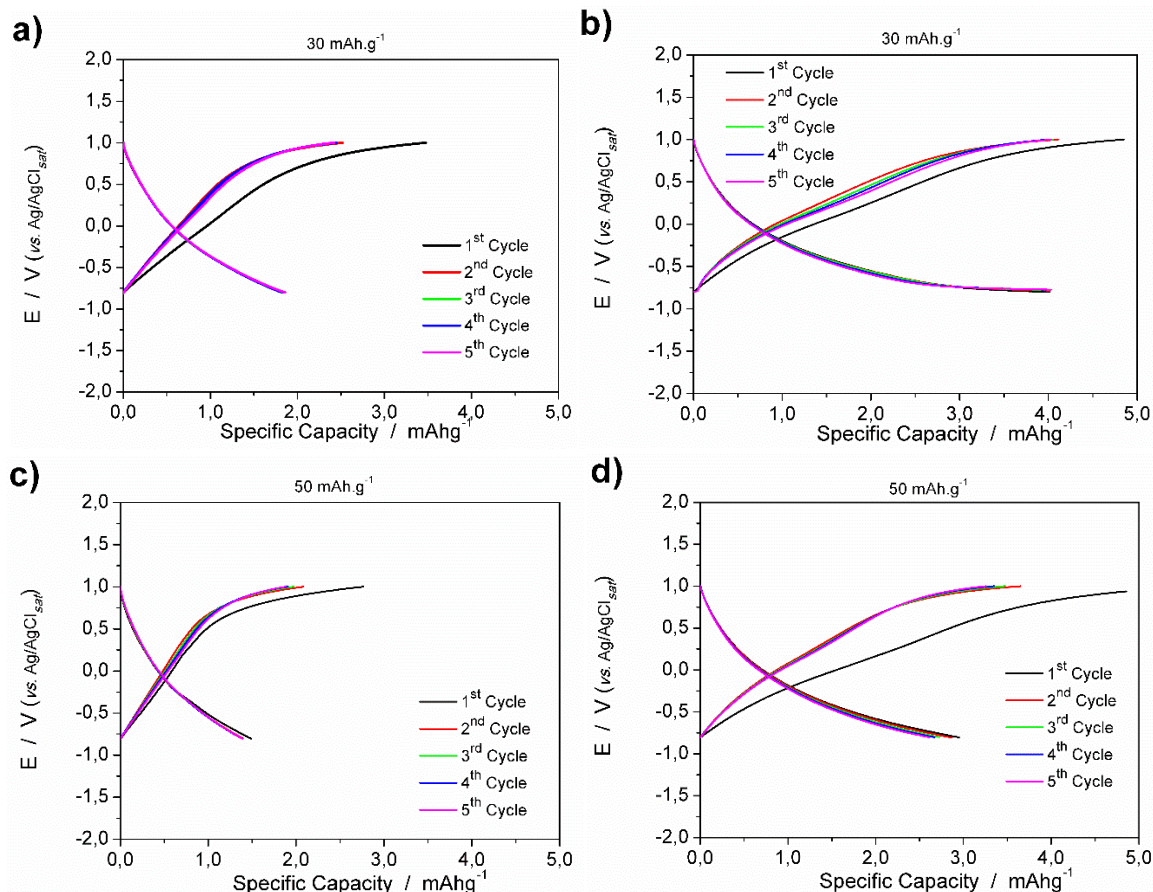


Fig. 9. Nyquist Diagrams for the electrochemical impedance spectroscopy (EIS) results for the Carbon Black (used for the electrode assembly), $\text{H}_2\text{Si}_4\text{Nb}_{16}\text{O}_{56}$ and $\text{H}_2\text{Si}_4\text{Nb}_{16}\text{O}_{56}\text{-GO}$: a), before Charge-Discharge Cycles and b) after Charge-Discharge Cycles.

Figure 10 shows the electrochemical performance at a galvanostatic cycling in a three electrodes cell considering half battery cells for SIBs. The C-D measurements were performed at three different current density, 30.0, 50.0 and 200.0 mA g^{-1} . It is observed that, with the increase in current density the C-D capacity decreases. The specific capacitance for the pristine material increased from approximately 2 to 4 mAh g^{-1} for the composite material at a current density of 30 mAh g^{-1} . For a current density of 50 mAh g^{-1} , the capacitance increased from 1.5 to 3 mAh g^{-1} , and at 200 mAh g^{-1} , it increased from 1.3 to 1.8 mAh g^{-1} . As discussed for VC

measurements it can be observed that the first charge process is different from the others. This behavior is assigned to the SEI formation. For the cycles from second to the fifth present a reasonable stability. Moreover, it clear that the composite material presents a potential plateau could be observed from the curve of 30 and 50 mA g^{-1} , further suggesting that the total capacity is originated from two different phenomena: the capacitive current and the pseudocapacitive process due to the presence of the $\text{H}_2\text{Si}_4\text{Nb}_{16}\text{O}_{56}\text{-GO}$ material.



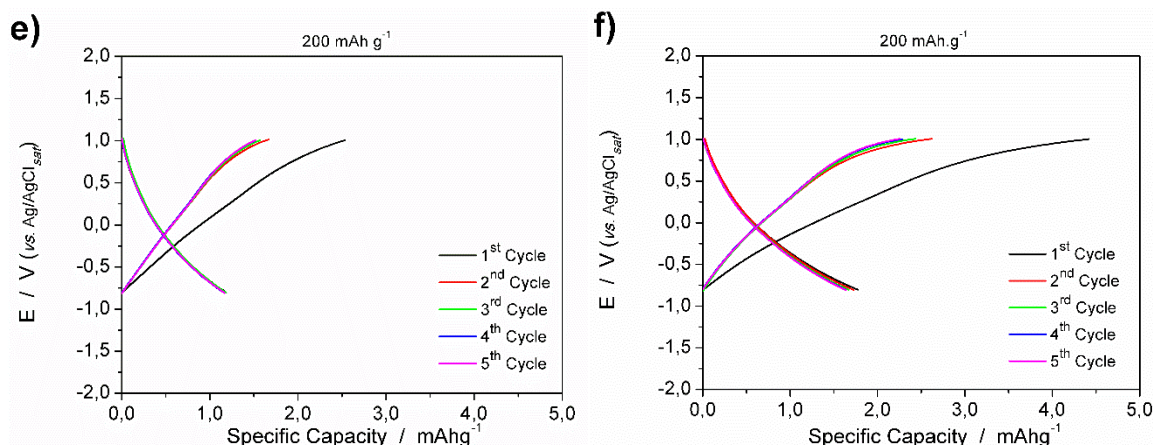


Fig. 10. Charge-Discharge measurements at different current density for a), c) e) pristine $\text{H}_2\text{Si}_4\text{Nb}_{16}\text{O}_{56}$ and for b), d) e) f) $\text{H}_2\text{Si}_4\text{Nb}_{16}\text{O}_{56}$ -GO composite.

4. Conclusions

In summary, this research successfully synthesized and characterized a Keggin-Type polyoxoniobate compound for potential application in sodium-ion batteries (SIBs). The results of structural characterization demonstrated the successful synthesis of the compound, with X-ray diffraction patterns, Raman spectroscopy, and FTIR spectra confirming its purity and integrity. Scanning electron microscopy analysis revealed the unique morphology of the composite material, indicating interactions between graphene oxide (GO) and polyoxoniobates. Elemental analysis further confirmed the composition of the composite material, aligning with the expected stoichiometry. Electrochemical characterization using various techniques, including cyclic voltammetry, chronopotentiometry charge/discharge, and electrochemical impedance spectroscopy, provided valuable insights into the electrochemical behavior of the synthesized material. It was observed that the $\text{H}_2\text{Si}_4\text{Nb}_{16}\text{O}_{56}$ -GO composite outperformed pure $\text{H}_2\text{Si}_4\text{Nb}_{16}\text{O}_{56}$, exhibiting higher electrochemical capacity and faster response due to the presence of graphene oxide. In summary, this study explored the synthesis and characterization of a Keggin-Type polyoxoniobate compound as a potential electrode material for sodium-ion batteries. The comprehensive analysis of its structure, morphology, and electrochemical behavior sheds light on its suitability for use in sustainable energy storage solutions, opening up new possibilities for the development of high-performance SIBs. The findings of this work contribute to the understanding of structure-activity relationships in polyoxoniobates and their potential as crucial components in future SIBs.

Acknowledgments

A.F.Y.M. acknowledges the financial support provided by the Conselho Nacional de Desenvolvimento Científico e Tecnológico (CNPq – Brazil) – Post-PhD research grant (Grant number 151838/2022-4). J.V.R.N. and J.R.G. acknowledge the financial support provided by the Conselho Nacional de Desenvolvimento Científico e Tecnológico (CNPq – Brazil) – Post-PhD research grant (Grant number 402826/2022-1).

Author Contributions

Alan F.Y. Matsushita: Conceptualization, Data curation, Formal analysis, Investigation, Methodology, Validation, Writing – original draft. João M.A. Leite: Data curation, Formal analysis, Methodology, Writing – original draft. Josias do R.V. do Nascimento: Data curation, Formal analysis, Methodology, Validation, Writing – original draft. Jarem R. Garcia: Conceptualization, Data curation, Formal analysis, Funding acquisition, Investigation, Methodology, Resources, Supervision, Validation, Visualization, Writing – original draft, Writing – review & editing.

References and Notes

- [1] Wen, Y.; He, K.; Zhu, Y.; Han, F.; Xu, Y.; Matsuda, I.; Ishii, Y.; Cumings, J.; Wang, C. *Nat. Commun.* **2014**, *5*, 4033. [\[Crossref\]](#)
- [2] Luo, W.; Shen, F.; Bommier, C.; Zhu, H.; Ji, X.; Hu, L. *Acc. Chem. Res.* **2016**, *49*, 23. [\[Crossref\]](#)
- [3] Zhang, W.; Zhang, F.; Ming, F.; Alshareef, H. N. *EnergyChem* **2019**, *1*, 100012. [\[Crossref\]](#)
- [4] Lu, W.; Wang, Z.; Zhong, S. *J. Phys. Conf. Ser.* **2021**, *2109*, 12004. [\[Crossref\]](#)
- [5] Cao, D.; Sha, Q.; Wang, J.; Li, J.; Ren, J.; Shen, T.; Bai, S.; He, L.; Song, Y.-F. *ACS Appl. Mater. Interfaces.* **2022**, *14*, 22186. [\[Crossref\]](#)
- [6] Priyadarshini, M.; Shanmugan, S.; Kirubakaran, K. P.; Thomas, A.; Prakash, M.; VEDIAPPAN, K. *RSC Adv.* **2021**, *11*, 19378. [\[Crossref\]](#)
- [7] Hartung, S.; Bucher, N.; Chen, H.-Y.; Al-Oweini, R.; Sreejith, S.; Borah, P.; Yanli, Z.; Kortz, U.; Stimming, U.; Hoster, H. E.; Srinivasan, M. *J. Power Sources.* **2015**, *288*, 270. [\[Crossref\]](#)
- [8] Jiao, L.; Dong, Y.; Xin, X.; Qin, L.; Lv, H. *Appl. Catal. B* **2021**, *291*, 120091. [\[Crossref\]](#)
- [9] Yang, Z.-X.; Huang, P.; Zhao, L.; Zhang, M.; Zhang, Y.-T.; Su, Z.-M. *Inorg. Chem. Commun.* **2014**, *44*, 195. [\[Crossref\]](#)
- [10] Lavall, R. L.; de Oliveira, P. S. C.; Ortega, P. F. R.; Trigueiro, J. P. C.; Gabriel, J. B.; Heitmann, A. P.; Chagas, P.; Oliveira, C. C.; Oliveira, L. C. A. *Chem. Eng. J.* **2023**, *455*, 140511. [\[Crossref\]](#)
- [11] Wawrzynczak, A.; Nowak, I.; Feliczak-Guzik, A. *Front.*

- Chem.* **2018**, 6, 560. [\[Crossref\]](#)
- [12] Priyadarshini, M.; Shanmugan, S.; Kirubakaran, K. P.; Thomas, A.; Prakash, M.; Senthil, C.; Lee, C. W.; Vediappan, K. *J. Phys. Chem. Solids* **2020**, 142, 109468. [\[Crossref\]](#)
- [13] Hartung, S.; Bucher, N.; Chen, H.-Y.; Al-Oweini, R.; Sreejith, S.; Borah, P.; Yanli, Z.; Kortz, U.; Stimming, U.; Hoster, H. E.; Srinivasan, M. *J. Power Sources* **2015**, 288, 270. [\[Crossref\]](#)
- [14] Yang, G.; Wu, Y.; Lv, Z.; Jiang, X.; Shi, J.; Zhang, Y.; Chen, M.; Ni, L.; Diao, G.; Wei, Y. *Chem. Commun.* **2023**, 59, 788. [\[Crossref\]](#)
- [15] Liu, J.; Chen, Z.; Chen, S.; Zhang, B.; Wang, J.; Wang, H.; Tian, B.; Chen, M.; Fan, X.; Huang, Y.; Sum, T. C.; Lin, J.; Shen, Z. X. *ACS Nano* **2017**, 11, 6911. [\[Crossref\]](#)
- [16] Nyman, M.; Bonhomme, F.; Alam, T. M.; Rodriguez, M. A.; Cherry, B. R.; Krumhansl, J. L.; Nenoff, T. M.; Sattler, A. M. *Science* **2002**, 297, 996. [\[Link\]](#)
- [17] Achee, T. C.; Sun, W.; Hope, J. T.; Quitzau, S. G.; Sweeney, C. B.; Shah, S. A.; Habib, T.; Green, M. J. *Sci. Rep.* **2018**, 8, 14525. [\[Crossref\]](#)
- [18] Parvez, K.; Wu, Z. S.; Li, R.; Liu, X.; Graf, R.; Feng, X.; Müllen, K. *J. Am. Chem. Soc.* **2014**, 136, 6083. [\[Crossref\]](#)
- [19] Loudiki, A.; Matrouf, M.; Azrioui, M.; Farahi, A.; Lahrach, S.; Bakasse, M.; El Mhammedi, M. A. *Appl. Surf. Sci. Adv.* **2022**, 7, 100195. [\[Crossref\]](#)
- [20] Coroş, M.; Pogăcean, F.; Roşu, M.-C.; Socaci, C.; Borodi, G.; Mageruşan, L.; Biriş, A. R.; Pruneanu, S. *RSC Adv.* **2016**, 6, 2651. [\[Crossref\]](#)
- [21] Surekha, G.; Krishnaiah, K. V.; Ravi, N.; Suvarna, R. P. *J. Phys. Conf. Ser.* **2020**, 1495, 12012. [\[Crossref\]](#)
- [22] Arifin, M.; Abdillah, O. B.; Maharsi, R.; Floweri, O.; Iskandar, F. *AIP Conf. Proc.* **2023**, 2623, 20004. [\[Crossref\]](#)
- [23] Prodan, D.; Moldovan, M.; Furtos, G.; Saroşi, C.; Filip, M.; Perhaiţa, I.; Carpa, R.; Popa, M.; Cuc, S.; Varvara, S.; Popa, D. *Appl. Sci.* **2021**, 11, 11330. [\[Crossref\]](#)
- [24] Ma, X.; Bian, Y.; Zhou, Y.; Zhao, Q.; Tian, Y.; Hua, J.; Ma, P. *J. Clust. Sci.* **2021**, 32, 613. [\[Crossref\]](#)
- [25] Son, J.-H.; Ohlin, C. A.; Casey, W. H. *Dalton Trans.* **2013**, 42, 7529. [\[Crossref\]](#)
- [26] Hong, T.; Wang, Y.; Nai, X.; Dong, Y.; Liu, X.; Li, W. *RSC Adv.* **2017**, 7, 53301. [\[Crossref\]](#)
- [27] Nguyen, V. T.; Le, H. D.; Nguyen, V. C.; Ngo, T. T. T.; Le, D. Q.; Nguyen, X. N.; Phan, N. M. *Adv. Nat. Sci.: Nanosci. Nanotechnol.* **2013**, 4, 35012. [\[Crossref\]](#)
- [28] Bleu, Y.; Bourquard, F.; Loir, A.; Barnier, V.; Garrelie, F.; Donnet, C. *J. Raman Spectrosc.* **2019**, 50, 1630. [\[Crossref\]](#)
- [29] Scardaci, V.; Compagnini, G. *C* **2021**, 7, 48. [\[Crossref\]](#)
- [30] Jehng, J. M.; Wachs, I. E. *Chem. Mater.* **1991**, 3, 100. [\[Crossref\]](#)
- [31] Ellis, J. E.; Sorescu, D. C.; Hwang, S. I.; Burkert, S. C.; White, D. L.; Kim, H.; Star, A. *ACS Appl. Mater. Interfaces.* **2019**, 11, 41588. [\[Crossref\]](#)
- [32] Hassan, M.; Walter, M.; Moseler, M. *Phys. Chem. Chem. Phys.* **2014**, 16, 33. [\[Crossref\]](#)
- [33] Gao, J.; Wang, C.; Chu, Y.; Han, Y.; Gao, Y.; Wang, Y.; Wang, C.; Liu, H.; Han, L.; Zhang, Y. *Talanta* **2022**, 240, 123197. [\[Crossref\]](#)
- [34] Vicentini, R.; Beraldo, R.; Aguiar, J. P.; Oliveira, F. E.; Rufino, F. C.; Larrude, D. R. G.; Da Silva, L. M.; Zanin, H. *J. Energy Storage* **2021**, 44, 103371. [\[Crossref\]](#)
- [35] Ding, Y.; Peng, J.; Khan, S.; Yuan, Y. *Chem. Eur. J.* **2017**, 23, 10338. [\[Crossref\]](#)

How to cite this article

Matsushita, A. F. Y.; Nascimento, J. R. V.; Leite, J. M. A.; Garcia, J. R. *Orbital: Electronic J. Chem.* **2025**, 17, 217.
DOI: <http://dx.doi.org/10.17807/orbital.v17i2.21046>